



HAL
open science

Investigation of liquid water heterogeneities in large area PEM fuel cells using a pseudo-3D multiphysics model

E. Tardy, F. Courtois, M. Chandesris, J.-P. Poirot-Crouvezier, A. Morin, Y. Bultel

► To cite this version:

E. Tardy, F. Courtois, M. Chandesris, J.-P. Poirot-Crouvezier, A. Morin, et al.. Investigation of liquid water heterogeneities in large area PEM fuel cells using a pseudo-3D multiphysics model. *International Journal of Heat and Mass Transfer*, 2019, 145, pp.118720. 10.1016/j.ijheatmasstransfer.2019.118720 . hal-04040379

HAL Id: hal-04040379

<https://hal.science/hal-04040379>

Submitted on 22 Mar 2023

HAL is a multi-disciplinary open access archive for the deposit and dissemination of scientific research documents, whether they are published or not. The documents may come from teaching and research institutions in France or abroad, or from public or private research centers.

L'archive ouverte pluridisciplinaire **HAL**, est destinée au dépôt et à la diffusion de documents scientifiques de niveau recherche, publiés ou non, émanant des établissements d'enseignement et de recherche français ou étrangers, des laboratoires publics ou privés.



Investigation of liquid water heterogeneities in large area PEM fuel cells using a pseudo-3D multiphysics model

E. Tardy^{a,b,*}, F. Courtois^{a,b}, M. Chandesris^a, J.-P. Poirot-Crouvezier^a, A. Morin^a, Y. Bultel^b

^a Univ. Grenoble Alpes, CEA, LITEN, F-38000 Grenoble, France

^b Univ. Grenoble Alpes, Univ. Savoie Mont Blanc, CNRS, Grenoble INP, LEPMI, F-38000 Grenoble, France

ARTICLE INFO

Article history:

Received 4 March 2019

Received in revised form 10 September 2019

Accepted 10 September 2019

Available online 24 September 2019

Keywords:

Proton Exchange Membrane Fuel Cell

Water transport

Two-phase flow

Computer simulations

Neutron imaging

ABSTRACT

Effective management of the liquid water and heat produced in Proton Exchange Membrane Fuel Cell (PEMFC) is necessary to increase both its performance and durability. In previous works, a pseudo-3D physic-based model of heat and water transport in fuel cells was developed and has been validated against experimental temperature and current density data. In this study, liquid water measurement obtained from neutron imaging tests is compared with numerical results. The model is able to predict qualitatively the presence of liquid water with a good accuracy taking into account the real Bipolar Plate (BP) design. Based on the reliability of the predictions at this first order in-plane space scale, the model has been used to compute the thickness of liquid water through the plane of the cell, in the different components of the stack, Gas Channel (GC) or Gas Diffusion Electrode (GDE). Our two-phase flow formulation has also been compared to more classical phase-separated two-phase flow model. A good accordance is observed for low saturations. The good agreement between predictions and measurement results supports the capability of our model to be employed in predictive control strategies or to design innovative Bipolar Plate (BP) at lower cost compared to experimental tests.

© 2019 Elsevier Ltd. All rights reserved.

1. Introduction

The Proton Exchange Membrane Fuel Cell (PEMFC) is a promising candidate for clean and efficient energy conversion in many applications, either stationary or transportation [1]. Of the many barriers, cost and durability, namely 30 \$ kW⁻¹ and 5000 h as targeted by the US Department of Energy (DOE) for 2020 [1], represent two of the most significant challenges to achieving clean, reliable and cost-effective fuel cell systems. Effective management of the liquid water and heat produced in PEM fuel cells remains crucial to increase both its performance and durability. Ineffective water and heat management can lead either to liquid-phase water blockage and mass-transport-limited performance or to decreased proton conductivity because of dehumidification of the ionomer [2,3]. Furthermore, high liquid water content and high temperature are believed to increase several degradation mechanisms [4].

The study of the combined effects of the heat transfer and water transport is necessary at a component scale in different key areas as gas inlet/outlet, called « local scale » in the next sections, but also at the cell level. Indeed, in an industrial fuel cell stack, the thermal

and water distribution heterogeneities are greater than in laboratory single cells. The heterogeneities are particularly exacerbated due to the size of the system and are directly related to the design of the cooling circuit [5].

As regards modeling, many computational heat and water transport PEMFC complex models have been developed during the last years due to an ever higher computing power in order to obtain accurate results. Many researches were conducted to design PEMFC models at different scales, from one-dimensional to three-dimensional, from one single component to entire cell. Furthermore, due to complex and coupled physical phenomena within a fuel cell, computation models adopt different approaches such as the governing equations, the number of considered layers, or the boundary conditions.

Commercial models including fuel cell module have been developed these last years. Star CD[®] was the first CFD software to implement a fuel cell module. ANSYS Fluent[®], ANSYS CFX[®], AVL FIRE[®] and COMSOL Multiphysics[®] are the most commonly CFD software including fuel cell module. Recently, Kone et al. [6] has reviewed the main multiphase fuel cell models and commercial softwares used for PEM fuel cell model simulation. Fink and Fouquet [5] developed a 3D model using the AVL FIRE[®] fuel cell module. They identified some shortcomings, especially in the membrane transport model. As a result, researchers commonly develop their own

* Corresponding author at: Univ. Grenoble Alpes, CEA, LITEN, F-38000 Grenoble, France.

E-mail address: erwan.tardy@cea.fr (E. Tardy).

Nomenclature

Acronyms

BP	Bipolar Plate
DOE	Department of Energy
CL	Catalyst Layer
CW	Cooling Water
GC	Gas Channel
GDE	Gas Diffusion Electrode (GDL + MPL + CL)
GDL	Gas Diffusion Layer
MEA	Membrane Electrode Assembly
MPL	Micro-Porous Layer
NCNR	NIST Center for Neutron Research
NI	Neutron Imaging
NIST	National Institute of Standards and Technology
PEM	Proton Exchange Membrane
PEMFC	Proton Exchange Membrane Fuel Cell
RH	Relative Humidity

Prefix

a	anode
c	cathode

Subscripts

i	specie
sat	saturation value
H ₂ O	water
O ₂	oxygen
H ₂	hydrogen
G	gas
L	liquid
vap	vapor

model. Many reviews [7–15] established the state-of-the-art of computational modeling in PEM fuel cells this last years and discussed the models strengths and weaknesses.

According to the evolution and the current status of PEMFC models, there is a need of multiphase flow models in order to understand the water management in PEM fuel cells, avoiding invasive and expensive experiments [16], which are limited in resolution terms. Indeed, the performance and the degradations in a PEMFC are intrinsically linked to the local temperature and humidity [4,17] and consequently to the rate of water phase change. Among the first research publications with respect to multiphase modelling were Wang and Cheng [18]. Based on the multiphase mixture theory, Zhuge et al. [19] developed a three-dimensional gas/liquid two-phase flow model applied to a part region of the fuel cell. Results showed that the liquid water distribution is mostly in the cathode, and predicted cell performance decreases quickly at high current density due to the obstruction of liquid water to oxygen diffusion. Siegel [20] introduced a two-dimensional model inside the Gas Diffusion Layer (GDL) and demonstrated that the fluid temperature is overestimated by one-phase models if there is phase change. With a two-dimensional multicomponent mixture model in a porous cathode adjacent to a flow channel, Wang et al. [21] studied a threshold current density corresponding to first appearance of liquid water in order to evaluate the water distribution and transport at the membrane/cathode interface. A 2-D multicomponent transport model was developed by He et al. [22] to investigate the effects of the gas and liquid flow on the cathode performance. Phase change was also discussed by Wang et al. [23] and Basu et al. [24]. Anderson et al. [25] published a review of cell-scale multiphase flow modeling, including water management with a focus on phase-change and transport processes. More recently, Bednarek and Tsotridis [26] presented the possible limitations and difficulties associated with PEM single fuel cell modelling.

However, the water phase change phenomenon is still unclear in PEM system and the liquid water flow modeling remains sketchy on large cell design. Indeed, the compared results between the simulation and the observations of the liquid water distribution sometimes shows significant differences at the local scale. Consequently, it is necessary to improve models by deepening the description of two-phase flows, especially in the gas channels and under the rib.

The most effective techniques to quantify the water distribution in Operating PEMFC are Neutrons and X-Ray Radiography/Tomog-

raphy. The latter using synchrotron source allows the best time and spatial resolution giving some measurement of water saturation in the GDL and channels. However, because of the large absorption of X-Ray by metallic parts, the analysis is limited to specifically designed cell, far from being representative of real stack. Neutrons, thanks to its ability to deeply penetrate most of the metals and its large interaction with protons, offer the best way to probe water inside a stack. Nevertheless, even if high resolution in-plane neutron radiography [27] can be conducted to probe the through-plane water distribution with a spatial resolution around a few μm , this can only be achieved with cell having an active area and a geometry far from being representative of stack. To resume, water distribution on the full active area of an operating stack can only be quantified with through-plane neutron imaging [28], without any resolution at the component scale.

In previous works, a pseudo-3D physic-based model of heat and water transport in fuel cells was developed and validated against experimental temperature and current density data obtained from a sensor plate (printed circuit board) inserted in the middle of the stack [29]. By comparing the results to neutron imaging observations, this latter model is able to predict qualitatively the presence of liquid water in the plane of the active area with a good accuracy [30]. The model emphasizes the complexity of the water transport in the different component cells, and namely the water flow through the membrane. It is shown that the net water flux from cathode to anode is highly heterogeneous both at the cell scale and at the channel/rib scale.

Recently, Rizvandi and Yesilyurt [31] have developed in parallel a 3D model and a pseudo-3D model. They have shown that there is a very good agreement between both of them. They concluded that their pseudo 3D model, which is 40 times faster than the 3D model, is very accurate based on the comparisons of polarization curves against the ones obtained from the 3D model.

To go further, this new study is mainly dedicated to quantify the liquid water distribution at low temperature (65 °C) and low current density (0.25 A cm⁻²) in a five 220 cm² cells stack using the pseudo-3D multiphysics model with an improved formulation of the saturation allowing to quantitatively extract a realistic water content while only qualitative information on presence of liquid water was computed in former study. Comparison between simulated and measured water distribution allows establishing the robustness and reliability of the model to calculate quantitatively local water content. Afterward, for the first time, the model was used to quantify the liquid water thickness and saturation in each

component of the cell, namely the Gas Diffusion Electrode and the Gas Channels both anode and cathode side. Finally, the spatial heterogeneities of the liquid water are observed at a channel/rib scale ~~in~~ taking into account the real Bipolar Plate design.

In the following Section 2, the stack design and the water content measurement by neutron imaging are presented with the operating conditions tested. The model is then described with the presentation of conservation and transport equations and two-phase formulation in Section 3. The domain of the model is also discussed in Section 3 with comparison between the two-phase pseudo-3D formulation and more classical phase-separated two-phase flow models. Finally, experimental tests are compared to numerical results at the entire cell and channel/rib scale (Section 4).

2. Experimental

2.1. Stack design for technology neutron imaging

Neutron imaging, which is an in-situ non-invasive technique [30], has been used to quantify the liquid water thickness distribution over the cell area for several operating conditions. The design and composition of the stack (Fig. 1a) have been extensively described in Ref. [30]. Briefly, a dedicated five 220 cm² cells stack has been build. It is made of stamped stainless steel Bipolar Plates (BP) with parallel serpentine channels (Fig. 1b) and low neutron absorption gilded aluminum end-plates. It comprises home-made Membrane Electrode Assembly (MEA) composed of 25 μm thick reinforced perfluorosulfonic acid membrane, commercial Pt based Catalyst Layer (CL) with anode and cathode loading of 0.1 and 0.4 mg cm⁻² respectively, Sigracet 24BC from SGL Group as Gas Diffusion Layer (GDL) and a 45 μm thick Micro-Porous Layer (MPL) on both sides. Heavy water is used as coolant because of its low neutron absorption.

2.2. Water content measurement by neutron imaging

Neutron imaging was performed at the National Institute of Standards and Technology (NIST) Center for Neutron Research (NCNR), located in Gaithersburg, Maryland, and using the BT-2 beamline. The experimental setup is detailed in Ref. [30]. An amorphous silicon detector with 0.127 mm pixel pitch was used to record images with a field of view of 20 cm × 25 cm. Images were recorded continuously with an acquisition time of 1 Hz. Neutron images presented in this work were averages of 10 consecutive images recorded at 1 frame per second (fps) to reduce random shot noise [30], which is an effective neutron image rate of 0.1 fps. A dedicated post-treatment analysis was developed to quantify the amount of water from the images. Briefly, the image of the cell in operation (intensity i) is referenced to the dry cell image (intensity i_0) to attain a processed image of the water. For thin sections of water, the water thickness (t) can be approximately obtained from the Lambert-Beer Law (Eq. (1)):

$$t = -\frac{1}{\mu_w} \ln\left(\frac{i}{i_0}\right) \quad (1)$$

where μ_w [m⁻¹] is the water attenuation coefficient measured in the calibration experiment. More comprehensive details can be found in Refs. [32–35]. This routine makes it possible to determine water maps of the stack as illustrated and to draw water thickness profiles according to different sections of the cell (Fig. 2). Recall that the stack is composed of 5 cells which they are supposed to work identically, i.e. with the same water distribution, given the fact that the difference between the cell voltages remain negligible. To obtain the liquid water thickness in a single cell, we divide the value obtained on the stack by 5. Cut lines at 25% and 50% are presented in Fig. 2. They specifically represent the outlets (25% cut line) of the reactants/product and the middle of the cell (50% cut line). Note that negative values appear on the scale of the figures because of

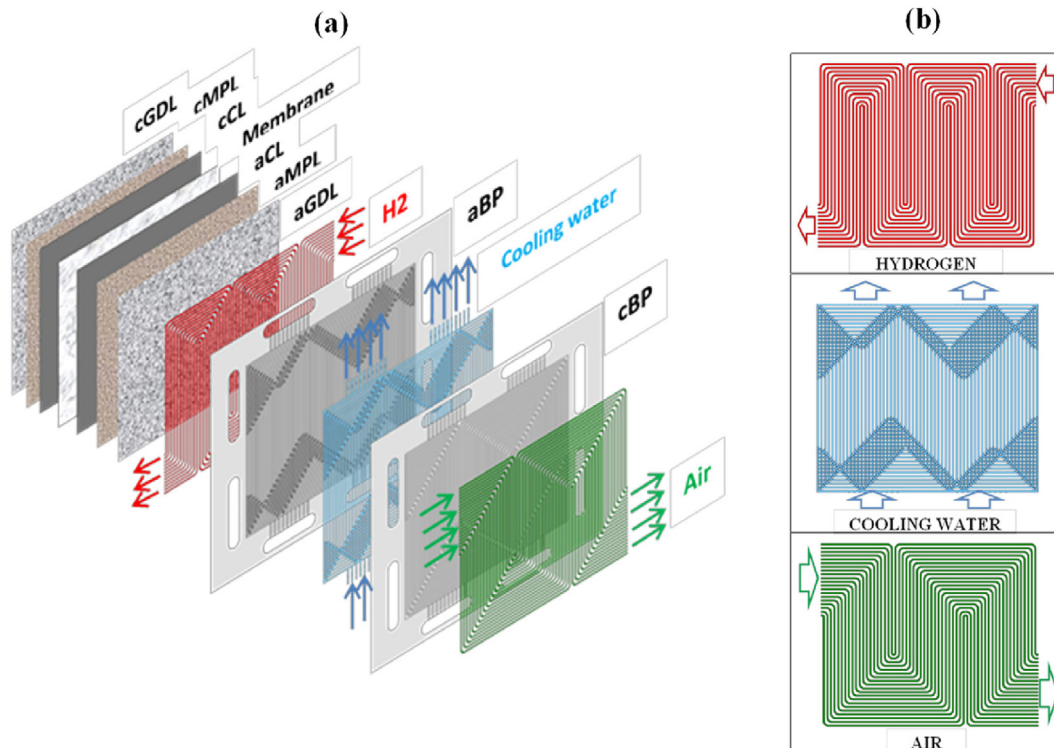


Fig. 1. (a) The reference geometry of the pseudo-3D model consists of 9 solid domains: one membrane, two catalyst layers (aCL and cCL), two micro-porous layers (aMPL and cMPL), two gas diffusion layers (aGDL and cGDL), two half-bipolar plates (aBP and cBP) – (b) Presentation of the flow fields: hydrogen, cooling water and air [30].

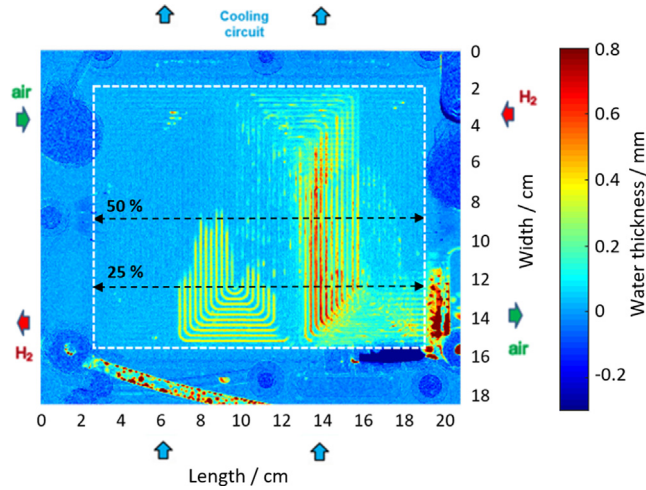


Fig. 2. Cartography of the water thickness after post-treatment analysis. The white box represents the active area (220 cm²) and the black dashed lines represent the lines used in the results section (4).

the presence of gas bubbles in the cooling circuits during the tests. It is clear that the saturation is never negative and null when the mixture is only in the gas phase.

2.3. Operation conditions

During the neutron imaging experiments, radiographies have been recorded varying the operating conditions, namely temperature, humidity, current density, pressure and gas stoichiometry to investigate their influence on the water distribution. In this study, we have focused our analysis on one operating conditions representative of humid state (Table 1) at a temperature of 65 °C with two current densities of 0.25 and 1 A cm⁻². The inlet temperature of the cooling water is set to maintain the outlet temperature equal to 65 °C. For example, in order to get this latter outlet temperature, the inlet temperature is respectively 64 °C and 59 °C for a current density of 0.25 and 1 A cm⁻². The difference is quite low because of the large flow of coolant.

3. Pseudo-3D multi-physics model

Physics-based PEMFC stack models of heat and water transfers are useful tools to investigate distribution of local conditions inside a stack. Since both temperature and liquid water distributions impact the degradation mechanisms, a pseudo-3D multiphysics model has been developed to predict at the cell scale the in-plane temperature and species distributions in all the components of the cell, including the cooling circuit [29]. It is well-known that the thickness of each component of the cell is very small compared to its length and width. Therefore, it can be appropriate to model the mass, species and heat transports using a pseudo-3D approach, considering each component of the cell as a plane layer, which exchanges species and heat out of plane with the adjacent components. So, the model considers the cell as a multilayered system and each layer is accurately in-plane discretized to allow the sim-

Table 1
Constant operating parameters.

Experimental parameters		Setpoint
Inlet pressure reactant gases/bar		1.5
Stoichiometry coefficient	Hydrogen	1.5
	Air	2
Relative humidity (%)	Hydrogen	50
	Air	50

ulation of local temperature and species heterogeneities, including liquid water. The transport equations are solved using this pseudo-3D approximation and coupled to an analytical electrochemical model to determine the local current density as function of the local conditions. The main advantage of the model is the prediction of the distributions of current density, species concentrations, water content and temperature in all the components of the cell with a low computation time compared to a full 3D model, while taking into account the real flow-field designs.

3.1. Geometrical domain and conservation equations

The pseudo-3D description is obtained by considering each component of the cell as a 2D layer. The classical 3D conservation equations are thus integrated over the thickness of each component, in order to obtain 2D conservation equations in each layer which includes non-classical source terms representing the flux exchanges between the different layers. The geometrical domain thus consists of 9 domains (see Fig. 1). For more details, the up-scaling approach is longer described in a previous work [30].

3.1.1. Pseudo-3D formulation of the conservation equations

With this approach [29], the full 3D model becomes the pseudo-3D model by introducing the in-plane velocity (\vec{v}), the in-plane mass fraction (w_i) and the in-plane temperature (T) (which are averaged values along the thickness). By coupling the in-plane variables through diffusion and/or convection fluxes ($\Sigma\phi$, $\Sigma\phi$) across the interfaces of the different components, it is possible to compute the 2D governing equations in each component. The governing equations are presented below. The model considers ideal gases for the reactants.

The equation of continuity (Eq. (2)) is solved on both the anode and cathode compartment (GC-GDL-MPL-CL) and in the Cooling Water (CW) channels. By considering a plug-flow with a uniform velocity, the Navier-Stokes momentum equation can be reduced to the Darcy law (Eq. (3)) for GC-GDL-MPL-CL in both side and the Darcy-Forcheimer law including a viscous shear stress term (Brinkman's term) (Eq. (4)) in the CW [36]. As a result, the computation time is acceptable while keeping accurate results [29]. The Forcheimer and Brinkman terms are considered to take into account the non-linearity of the losses due to the consecutive section changes in the CW channels.

$$\nabla_{2D} \cdot (\rho \varepsilon \vec{v}) = \Sigma\phi + \Sigma\phi + S_m \quad (2)$$

$$\nabla_{2D} p = \frac{1}{K_1} \mu \vec{v} \quad (3)$$

$$\nabla_{2D} \cdot \mu (\nabla_{2D} \vec{v} + (\nabla_{2D} \vec{v})^T) + \nabla_{2D} p = \frac{1}{K_1} \mu \vec{v} + \frac{1}{K_2} \|\vec{v}\| \vec{v} \quad (4)$$

where ρ is the mixture density, ε , the porosity, S_m , the local mass source, μ , the dynamic viscosity, K_1 and K_2 the hydraulic permeability and passability coefficients. The equation of species conservation (Eq. (5)) is solved in each layer except in the cooling circuit. Note that the equation of the species conservation is solved for $i-1$ species since the mixture density is calculated from the continuity equation. Indeed, the density of the last specie is deduced by difference of the mixture density and the density of other species.

$$\nabla_{2D} \cdot (\rho \varepsilon w_i \vec{v}) = -\nabla_{2D} J_i + \Sigma\phi_i + \Sigma\phi_i + S_{i,m} \quad (5)$$

Where w_i , J_i and $S_{i,m}$ are respectively the species mass fraction, the species diffusion flux and the local species source. The heat transport equation is represented by Eq. (6) in all components.

$$\vec{v} \cdot \nabla_{2D} (\rho c_p T) = \lambda \nabla_{2D}^2 T + \Sigma\phi_T + \Sigma\phi_T + S_T \quad (6)$$

where c_p , λ and S_T are respectively the heat capacity, the thermal conductivity and the local heat source. The conservation equations are resolved according to the different layers (Table 2).

3.1.2. Electro-chemical model

For the electrical response, a semi-empirical electro-chemical model is adopted which is coupled to the conservation equations at the membrane/CL interface [29]. The cell potential setpoint is obtained by the following equation (Eq. (7)):

$$U_{cell} = E_{rev} + \eta_{act} + \eta_{ohm} \quad (7)$$

where E_{rev} , η_{act} and η_{ohm} are respectively the Nernst reversible potential of the cell, the reaction overpotential and the ohmic losses. Those three terms are detailed by Eqs. (8)–(10).

$$E_{rev} = a_1 + a_2 T + a_3 T \ln(P_{O_2}) + a_4 T [\ln(P_{H_2}) - \ln(P_{H_2O})] \quad (8)$$

$$\eta_{act} = \beta_1 + \beta_2 T + \beta_3 T \ln(i) + \beta_4 T \ln(P_{O_2}) + \beta_5 T \ln(P_{H_2O}) + \beta_6 T \ln(P_{H_2}) \quad (9)$$

$$\eta_{ohm} = -(R_e + R_p) i \quad (10)$$

where P_i is the partial pressure of the species, i , the current density, R_e the cell electrical and R_p the protonic resistances. The physical parameters a_i and β_i are dependent on the thermodynamics and the kinetics of the electrochemical reactions. The model considers uniform cell potential along the cell surface.

3.1.3. Source terms

For the heat transport equation, the source term in the cell (Eq. (11)) is obtained by considering the total energy balance. It corresponds to the difference between the total power and the electrical power produced:

$$S_T = \left(\frac{\Delta H_0}{2F} - U_{cell} \right) i \quad (11)$$

where ΔH_0 , is the enthalpy variation of the electrochemical reaction in the reference conditions, F , the Faraday constant and U_{cell} the cell potential. Note that the heat source depends directly on the current density distribution.

The heat (or enthalpy variation) ΔH_0 depends on the phase of the produced water (vapor or liquid). Indeed, a possible phase change of the water can take place in each component where gaseous media is considered. To avoid a complex two-phase model, an approximation of the phase change of the water has been implemented.

In all the components, a hypothetical water vapor partial pressure P_{H_2O} is calculated from the continuity and momentum equations. This hypothetical water is considered in the model as a perfect gas that cannot be liquefied. With this hypothesis, both liquid and vapor phases are assimilated to water vapor in the transport equation. Thus, this hypothetical pressure can be higher than the saturation pressure of water $P_{sat}(T)$, fixed by the equilibrium pressure of vapor in the presence of liquid water, which depends only on local temperature T . If the hypothetical water vapor pressure P_{H_2O} is lower than the saturation pressure $P_{sat}(T)$, there is only vapor phase in the layer and, $P_{vap} = P_{H_2O}$ where P_{vap} is the practical water vapor pressure. Otherwise, liquid water is

present and, $P_{vap} = P_{sat}(T)$. Finally, the reaction enthalpy variation can take two different values:

$$\Delta H_0 = \begin{cases} \Delta H_v = 242 \text{ kJ mol}^{-1} & \text{if } P_{H_2O} \leq P_{sat}(T) \\ \Delta H_l = 285.8 \text{ kJ mol}^{-1} & \text{if } P_{H_2O} = P_{sat}(T) \end{cases} \quad (12)$$

where ΔH_v and ΔH_l are respectively the enthalpy variation assuming vapor and liquid phase of the water.

3.1.4. Water transport through the membrane

Water transport depends on two distinct phenomena: the electro-osmosis drag and the molecular diffusion. The water electro-osmotic drag flux (Eq. (13)) through the membrane is the movement of liquid water molecules induced by an applied potential (ionic current). The flux of water dragged from anode to cathode is:

$$F_{eo} = \frac{a_{eo} M_{H_2O} i}{F} \quad (13)$$

where a_{eo} and M_{H_2O} are respectively the electro-osmotic drag coefficient and the molecular mass of the water. The electro-osmotic drag coefficient depends exclusively on the water content. However, there are several formulations of this coefficient in the literature. Among them, Springer et al. [37] proposed a linear relation, Hwang et al. [38] and Meier et al. [39] considered a quadratic evolution and Zawodzinski et al. supposed a discontinuous relation [40]. These laws are presented in Table 3.

Where λ_M is the averaged number of water molecules per sulfonic acid group, also called membrane water content. The water content is observed and discussed in details in Ref. [4] with post-mortem analysis of the MEAs and Bipolar Plates. Furthermore, the liquid water molecules can be diffused across the membrane both from the anode to the cathode and from the cathode to the anode depending on the sign of the concentration gradient. The diffusive flux (Eq. (14)) are designed by considering a Fick's law:

$$J_{diff} = D_m \frac{M_{H_2O}}{e_m} c_f (\lambda_{aCL}(a) - \lambda_{cCL}(a)) \quad (14)$$

where e_m is the membrane thickness, c_f , the molar concentration of sulfonate sites in Nafion, λ_{aCL} and λ_{cCL} , the anode and cathode CL water contents and a the water activity. The water content at the interfaces between the Nafion and the pores of the catalyst layers (λ_{aCL} and λ_{cCL}) depends on the activity, a , using the Springer's law. According to Eq. (14), the diffusive flux is considered positive ($\lambda_{aCL} > \lambda_{cCL}$) from the anode to the cathode and negative from the cathode to the anode ($\lambda_{aCL} < \lambda_{cCL}$). Different models for the membrane water diffusivity D_m are proposed in the literature. The laws proposed by Fuller [41], Zawodzinski et al. [42] and Motupally et al. [43] are presented in Table 4. The diffusion coefficient depends on the water content and the temperature. A sensitivity analysis of these coefficients is presented in the Section 4.1.

3.2. Condensation model

A phase change of water can take place in each subsystem where the gaseous media are considered. A two-phase flow model should be considered to accurately simulate phase changes. However, two-phase flow transport formulation can require high com-

Table 2
Conservation equations in each layer.

Component	Continuity	Darcy	Darcy-Forcheimer with Brinkman's term	Species conservation	Heat transport
GCs	•	•		•	•
GDLS, MPLs, CLs	•	•		•	•
CW channels	•		•		•

Table 3
Electro-osmosis drag coefficients.

Author(s)	Equation
Springer [37]	$a_{eo} = \frac{2.5\lambda_M}{22}$
Hwang et al. [38]	$a_{eo} = -3.4 \cdot 10^{-19} + 0.05\lambda_M + 0.0029\lambda_M^2$
F. Meier et al. [39]	$a_{eo} = 1 + 0.028\lambda_M + 0.0026\lambda_M^2$
Zawodzinski et al. [40]	$a_{eo} = \begin{cases} 1 & \text{if } \lambda_M \leq 14 \\ 0.1875\lambda_M - 1.625 & \text{if } \lambda_M > 14 \end{cases}$

putation resources and complex numerical schemes. Therefore, a two-phase flow simplification has been developed in this study, based on preliminary test performed in [29].

As described above, a hypothetical water vapor partial pressure P_{H_2O} is calculated in all the components. This hypothetical pressure is not limited to the saturation pressure $P_{sat}(T)$. By considering both liquid and vapor phases assimilated to water in the transport equation, a post-treatment of the data is required to analyze the simulation results regarding the local water content in each layer of the cell. Then, it is necessary to calculate the water saturation s to evaluate the amount of water in the liquid phase. The water saturation depends on the values of the P_{H_2O} . Indeed, if the saturation pressure is reached, it is assumed that water is produced in liquid phase and the water saturation is calculated thanks to Eq. (15). Otherwise it is in vapor phase, considering a water saturation equal to zero.

$$\begin{cases} s = 0 & \text{if } P_{H_2O} \leq P_{sat}(T) \\ s = \frac{P_{H_2O} - P_{sat}(T)}{P - P_{sat}(T)} & \text{if } P_{H_2O} \geq P_{sat}(T) \end{cases} \quad (15)$$

where P is the total pressure of the gas mixture.

The simulation results are post-treated to evaluate the local water content in each layer of the cell, together with the local saturation s_i . In order to obtain the thickness of the liquid water in each layer, the saturation calculated in a layer is multiplied by the layer porosity, ε_i and the layer thickness, e_i , regardless of the flow type of the liquid water. The total thickness in the whole cell (Eq. (16)), to be compared to the Neutron Imaging results is therefore the sum of its products in each layer:

$$e_w = \sum \varepsilon_i e_i s_i \quad (16)$$

Note that a porosity of one is taken for gas channels. The thickness of liquid water in the membrane is negligible compared to those in the other components.

3.3. Pseudo-3D and phase-separated models

3.3.1. Relationship between both models

A comparison of the saturation equation seen above with a more classical formulation will be discussed in this section. We consider two models: an empirical model with phase-separated flow proposed by Lockhart-Martinelli [44] and the pseudo-3D model presented in this study. For the first model, the saturation s_l is defined as the fraction of the volume occupied by the liquid, and the model allows to compute both the liquid, $u_{L,1}$, and gas, $u_{G,1}$, velocities. For the second model, only one mixture velocity

is computed which corresponds to both the gas velocity $u_{G,2}$ and the condensed vapor velocity $u_{vap,2c}$, while the saturation s_2 is deduced from the formulation presented in Section 3.2. To compare the two models, a flow of moist air (non-depleted in oxygen) in a channel is studied assuming no production or consumption of species by analyzing the velocities obtained by both formulations when their saturations are equal, i.e. $s_1 = s_2 = s$. The velocities can be expressed as follows (Eqs. (17)–(20)):

$$u_{G,1} = \frac{\dot{m}_G}{\rho_G A_c (1 - s_1)} \quad (17)$$

$$u_{G,2} = \frac{\dot{m}_G}{\rho_G A_c (1 - s_2)} \quad (18)$$

$$u_{L,1} = \frac{\dot{m}_L}{\rho_L A_c s_1} \quad (19)$$

$$u_{vap,2c} = \frac{\dot{m}_{vap,c}}{\rho_{vap,c} A_c s_2} \quad (20)$$

where ρ_G , ρ_L , $\rho_{vap,c}$ are respectively the gas, liquid and condensed vapor density, \dot{m}_G , \dot{m}_L , $\dot{m}_{vap,c}$ the gas, liquid and condensed vapor mass flow rate, A_c and s the channel section and the saturation. With the pseudo 3D approach, the flow is considered homogeneous, i.e. $u_{G,2} = u_{vap,2c}$ and we can assume $\dot{m}_L = \dot{m}_{vap,c}$. If the saturations are equal, we obtain $u_{G,1} = u_{G,2} = u_G$. We can then deduce the ratio of gas/liquid velocities S (Eq. (21)) as follows:

$$S = \frac{u_G}{u_{L,1}} = \frac{u_{vap,2c}}{u_{L,1}} = \frac{\rho_L}{\rho_{vap,c}} \quad (21)$$

This relation shows that, the pseudo-3D formulation corresponds to a phase separated model assuming a velocity slip ratio equals to the density ratio of water, i.e. 1055 in the considered operating conditions $P = 1.5$ bar and $T = 80$ °C. This value is rather high in comparison with more classical correlation, but corresponds to a quasi stagnant liquid phase ($u_{vap,2c}/u_{L,1} = 1055$). Indeed, the maximum velocities ratio S_{chi} proposed by Chisholm [45] is equal to 27.7 in the same operating conditions (Eq. (22)).

$$S_{chi} = \sqrt{1 - x \left(1 - \frac{\rho_L}{\rho_G}\right)} \quad (22)$$

where x is the gas quality (Eq. (23)).

$$x = \frac{\dot{m}_G}{\dot{m}_G + \dot{m}_L} \quad (23)$$

Note that the liquid water flow in the GC is slower than the liquid flow presented in the Chisholm model [45] that corresponds to a simple annular flow. The smaller hydraulic diameter, specific geometry and GDL porosity may explain this difference and therefore the higher velocities ratio in the GC compared to the Chisholm correlation.

To go further, equal pressure losses instead of equal saturations is considered between the two models. Using Eqs. (25) and (31) in

Table 4
Diffusion coefficients.

Author(s)	Equation
Fuller [41]	$D_m = 2.1 \cdot 10^{-7} \lambda_M \cdot \exp(-\frac{2436}{T})$
Zawodzinski et al. [42]	$D_m = (6.707 \cdot 10^{-8} \lambda_M + 6.387 \cdot 10^{-7}) \cdot \exp(-\frac{2416}{T})$
Motupally et al. [43]	$D_m = \begin{cases} 3.1 \cdot 10^{-7} \lambda_M [\exp(0.28\lambda_M) - 1] \cdot \exp(-\frac{2346}{T}) & \text{if } 0 \leq \lambda_M \leq 3 \\ 4.17 \cdot 10^{-8} \lambda_M [1 + 161 \cdot \exp(-\lambda_M)] \cdot \exp(-\frac{2346}{T}) & \text{if } 3 \leq \lambda_M \leq 17 \end{cases}$

Appendix, we can deduce a relationship between the two saturations s_1 and s_2 (Eq. (24)):

$$s_1 = \left(1 + 4S \frac{\mu_l}{\mu_g} \left[-C + \sqrt{C^2 - 4 \left(1 - \frac{\mu_2}{\mu_g} \frac{1}{1-s_2} \right)} \right]^{-2} \right)^{-1} \quad (24)$$

where S , μ_l , μ_g , μ_2 and C are respectively the gas/liquid velocities ratio, the liquid, gas and moist air dynamic viscosities and a coefficient dependent on the flow regime. A sensitivity analysis to the gas/liquid velocities ratio S is detailed in the Supplementary material.

3.3.2. Sensitivity analysis to C parameter

There are several formulations of the coefficient C in the literature, which is dependent on the flow regime. For a laminar flow for both the gas and liquid phase, Lockhart-Martinelli [44] recommend $C = 5$ while Chisholm [45] proposes $C = 2.5$. Kim and Mudawar [46], Mishima and Hibiki [47], Zhang et al. [48], Li and Wu [49] suggest an equation of C parameter dependent on dimensionless numbers. Other correlations are proposed in Ref. [50].

On most current bipolar plates, the hydraulic diameter of a channel varies from $4 \cdot 10^{-4}$ to $6 \cdot 10^{-4}$ m. For current densities of about 1 A cm^{-2} , the Reynolds number for the gas is less than 500, and most often between 250 and 300. Regarding the liquid phase, the flow has a much lower velocity than the gas phase, and consequently the Reynolds number for the liquid water is also much lower than the Reynolds number of the gas phase. This is why the flows are always considered laminar in the reaction channels.

Fig. 3 presents the evolution of s_1 as a function of s_2 according to Eq. (24) with different values of C and S equal to 1055. The parameter $C = 5$ gives the closest correspondence between the two models if we take into account the entire range of liquid saturation (from 0 to 1). Nevertheless, as noted by Kim and Mudawar [46], the value proposed by Lockhart-Martinelli [44] seems too high to correctly describe the two-phase flow at low saturation. The correlation proposed by Kim and Mudawar [46], Mishima and Hibiki [47], Zhang et al. [48] and Li and Wu [49] give good results at low saturation. A sensitivity analysis to the gas/liquid velocities ratio S is detailed in the Supplementary material. This analysis shows that, despite a high velocities ratio (see Fig. S1b in the D

Supplementary material), the saturations obtained by the two models are close when we consider low saturation ($s < 0.1$).

The previous results showed a good coincidence between the empirical model with phase-separated flow and the pseudo-3D model assuming equal pressure drop between the two models, especially for low saturations. This may explain the good coincidence of the numerical results with the experimental tests since the saturation is relatively low (Fig. 7b). Nevertheless, the validity domain of the pseudo-3D model cannot be defined precisely.

4. Results and discussion

The thermal, fluid dynamic and electrochemical aspects of the model were validated in a previous work by comparison with local temperature and current densities measurements [29]. The pseudo 3D model is then able to predict the heterogeneous distribution of the current density and temperature in a large range of operating conditions. In this study, our work will be focused on the analysis of the accuracy and quantitative predictability of the two-phase flow formulation.

4.1. Sensitivity analysis to diffusive and drag coefficients

To compare the effect on the water distribution of the drag coefficient formulations presented in Table 3, the total liquid water thickness (averaged) for the five cells was plotted in a along the indicated reference cut line at 50% of the cell for a temperature of $65 \text{ }^\circ\text{C}$ at low current density and for a Motupally diffusion coefficient. The general pattern of the total liquid water thickness is not impacted by any of the formulations of the electro-osmosis drag coefficient. Nevertheless, the amplitude of the total thickness of liquid water can vary up to 0.14 mm maximum, which corresponds to 19% of the maximum water thickness measured or simulated. The coefficient proposed by Zawodzinski was retained in the previous study [29], and reused here. In addition, this coefficient is simple to implement in the code for $\lambda_M \leq 14$.

Similarly for the diffusion coefficient, the total liquid water thickness (averaged) was plotted in Fig. 4b along the indicated reference cut line at 50% of the cell to compare the different formulations presented in Table 4 for a Zawodzinski drag coefficient. These coefficients are the subject of many works. The profile of the curves

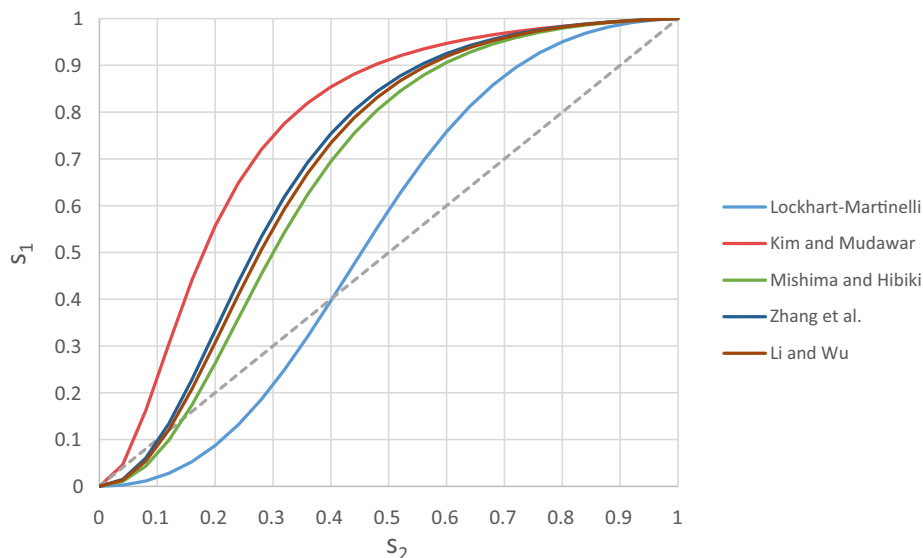


Fig. 3. Relation between the saturations s_1 and s_2 with different formulation of C parameter and S equal to 1055 – the dashed curve represents the exact equality of the saturations of the two models.

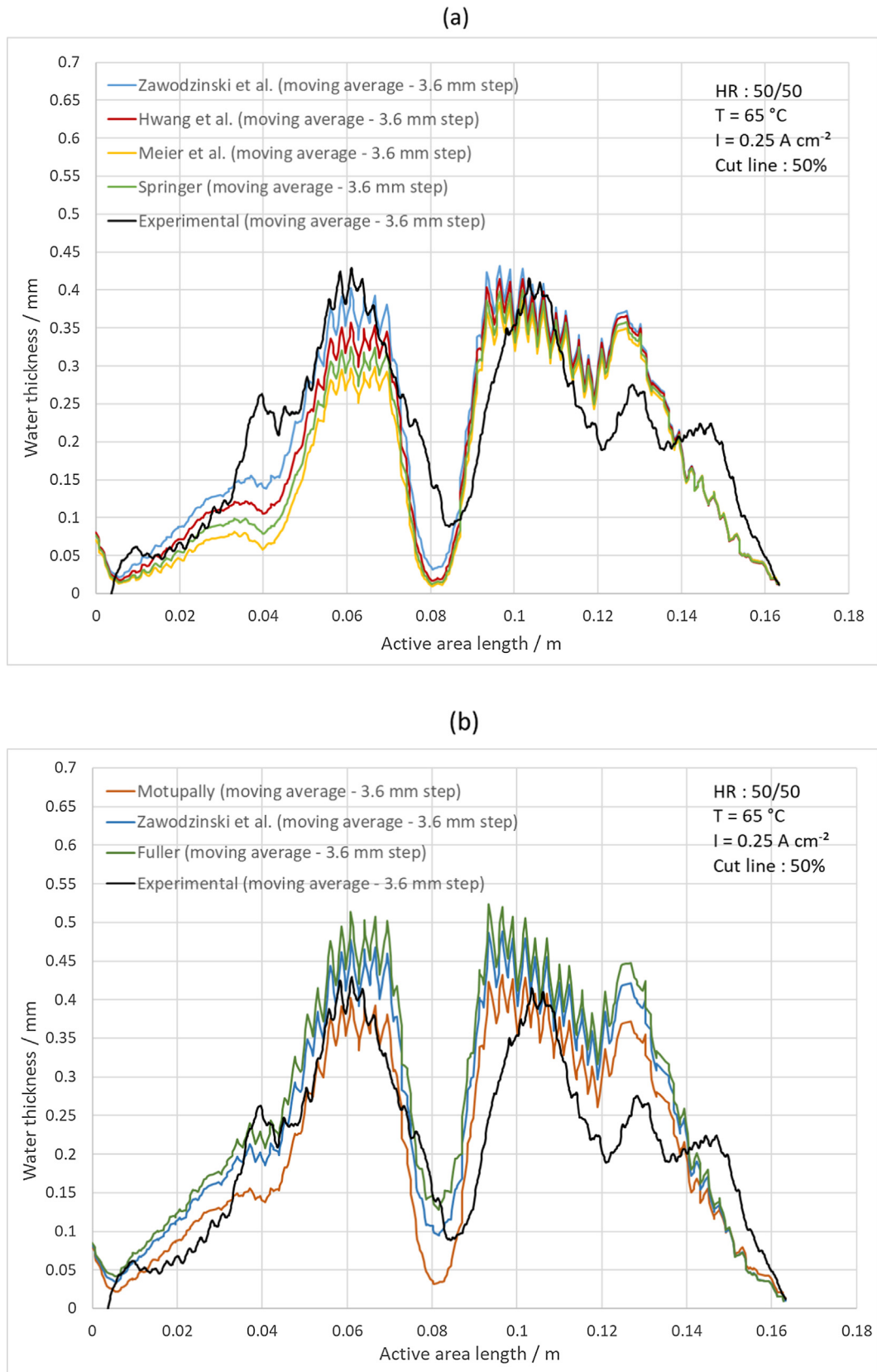


Fig. 4. Water thickness for the 5 cells of the stack simulated at the indicated 50% cut line in the operating conditions presented in Table 1 for a current density of 0.25 A cm^{-2} according to different formulations of the (a) electro-osmosis drag and the (b) diffusion coefficient.

is the same, with however still a non-negligible impact on the amplitude. The maximum difference is obtained between the Fuller and Motupally formulation, and reaches 0.17 mm, corresponding to 24% of the maximum water thickness measured or simulated. The coefficient proposed by Motupally was retained in the previous study [29], and reused here.

We can observe the same trends of the liquid water evolution in the stack in Fig. 3 even if there is variations that can appear important. This reflects the complexity of formulating the water transport within a PEMFC. Indeed, the electro-osmosis drag and the diffusion coefficients are key elements for modeling the transport of water through the membrane. An entire publication could be devoted to these coefficients, which is not the aim in this work.

4.2. Two-phase flow model validation

The distribution of the liquid water thickness observed for the stack composed of 5 cells for rather humid conditions, i.e. at low temperature stack 65 °C for a low/high current density is presented in Fig. 5. The liquid water distribution simulated as well as measured via neutron imaging is presented, where the color scale is related to the thickness of the liquid water. Both simulated and measured maps are obtained in the operating conditions detailed in the Table 1. At the whole cartography scale, for the low current

density, the model is able to accurately and quantitatively predict the liquid water areas in the stack (Fig. 5a and b). Despite the simplification of the present two-phase flow approach, the simulated values are very close to the measured ones. As a matter of fact, there is more liquid water accumulation in the cold zones according to the temperature distribution and close to the both gas outlets [29]. The mean value of this water thickness along the cell is 0.3 mm. Namely, it is lower close to the hydrogen inlet as well as air inlet and reaches its lowest value in the hot spots. For the high current density, the model is able to locate the liquid water in the stack. Nevertheless, the model overestimates the liquid water thickness at the hydrogen outlet and underestimates it at the air outlet. Furthermore, the model correctly represents the channel/rib pattern.

Fig. 6 presents the water thickness distribution (averaged) at the low current density along the indicated reference cut line at 50% of the cell, perpendicularly to the cooling water mainstream. The 1D plot at the different reference cut lines allows to better illustrate the differences in water content distribution in order to identify the main sources of water content heterogeneities. 25% cut line will be analyzed later. For the 50% reference cut line, the model is able to accurately predict water areas in comparison with neutron imaging. The oscillations over the line plots are related to the channel/rib heterogeneities.

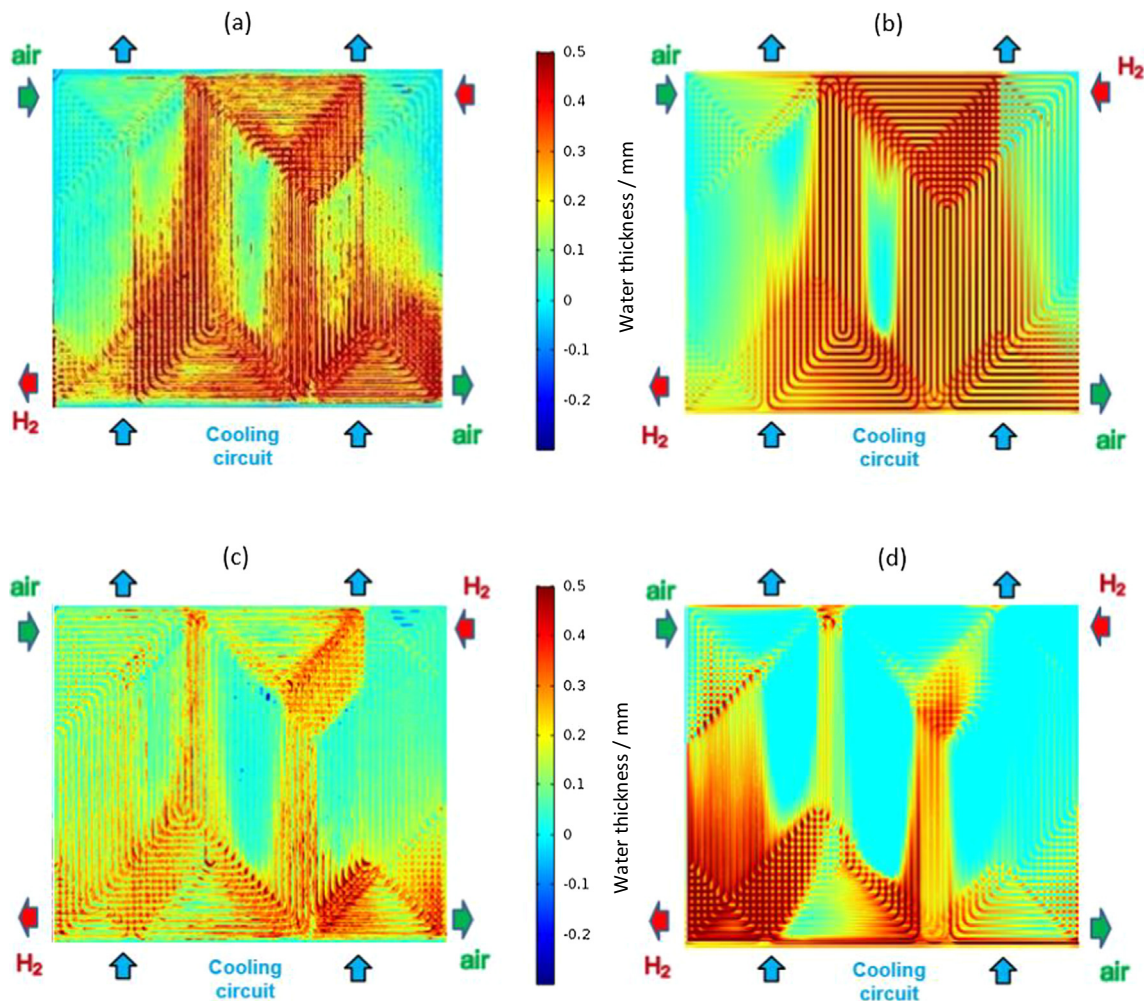


Fig. 5. (a) measured and (b) simulated total water thickness for 5 cells for a current density of 0.25 A cm^{-2} and for an inlet cooling water temperature of 64 °C – (c) measured and (d) simulated total water thickness for 5 cells for a current density of 1 A cm^{-2} and for an inlet cooling water temperature of 59 °C .

4.3. Water distribution over the cell surface in each layer

The main advantage of the pseudo-3D model is its ability to predict the liquid water distribution at the rib/channel scale in the different zones as well as in the different layers of the cell. The water thickness and saturation distribution in the anode and cathode Gas Channels (GC) and Gas Diffusion Electrode (GDE), in the operating conditions presented in the Table 1 for a current density of 0.25 A cm^{-2} is illustrated in Fig. 7. We can notice that both hydrogen and air inlet dry the anode and cathode GDE at the inlet because of the low RH of the gas flows. On the whole, liquid saturation as well as water thickness increases from the air inlet to the outlet at the cathode side because of the water production by the oxygen reduction reaction and electro-osmotic flux (Fig. 8a). Nevertheless, lower saturation and water thickness are observed in some areas because of hot spot induced by water cooling as mentioned in Ref. [29]. Fig. 8 shows the computed water fluxes across the membrane, which are the result of the balance between electro-osmotic drag (Fig. 8a) and molecular diffusion (Fig. 8b). The total flux is presented in Fig. 8c. In this figure, the positive values represent the flux from the anode to the cathode while the negative values represent the flux from the cathode to the anode. We can note that the electro-osmotic flux drives the water from the anode to the cathode whereas the diffusive flux can proceed in both directions according to the concentration of water in the cell. Indeed, an important diffusive flux (Fig. 8b) dries the anode GDE in the area close to the hydrogen inlet because the hydrogen is relatively dry (50% HR). This phenomena induces a local drying of the cathode GDE in this same region. So, the diffusive flux compensates the electro-osmotic flux (Fig. 8c) and drives exclusively the liquid water from the cathode to the anode. From a general point of view, the liquid water is more present in the cathode compartment where the water is produced (Fig. 7).

4.4. Water distribution at rib/channel scale

In this section, the saturation of liquid water and the total water flux are plotted at the rib/channel scale in the GC and the GDE both anode and cathode side in order to study the water distribution and the spatial heterogeneities. Both are observed along the indicated reference cut line at 25% of the cell, perpendicularly to the cooling water mainstream that corresponds to the air outlet (from x (active area length) = 12 to $x = 16.3 \text{ cm}$) in Fig. 9. The scale on the left represents the saturation of liquid water in the canal and/or under the rib. The saturation is considered positive on the anode side and negative on the cathode side. The right scale represents the pattern of the bipolar plate.

In the bipolar plate (Fig. 9a), the liquid water is concentrated inside the gas channels both the anode and cathode side which is an expected result. There is no water or very little at the very end of the air outlet on the anode side (from x (active area length) = 15.3 to $x = 16.3 \text{ cm}$). In the GDE (Fig. 9b) on both anode and cathode sides, the liquid water accumulates preferentially under the rib. Straubhaar et al. [51] demonstrated that the region in the GDL underneath the rib is globally colder than the region under the channel, that may explain a higher condensation in this area. We still find liquid water in the GDE in front of the channels. The oscillations that can be observed in the cathode GDE along the rib close to the cathode outlet (Fig. 9b) can be explained by the influence of the rib/channel pattern on the anode side. The total water flux is also impacted by the design of the cell. At the air outlet, where we find a succession of gas channels and rib on the anode side in front of a single rib on the cathode side, we can note a fluctuation of the flux. The flux is less important under the rib considering the anode pattern. Thus, water content in the cathode GDE is strongly impacted by the anode design. Finally, the flux is negative, i.e.

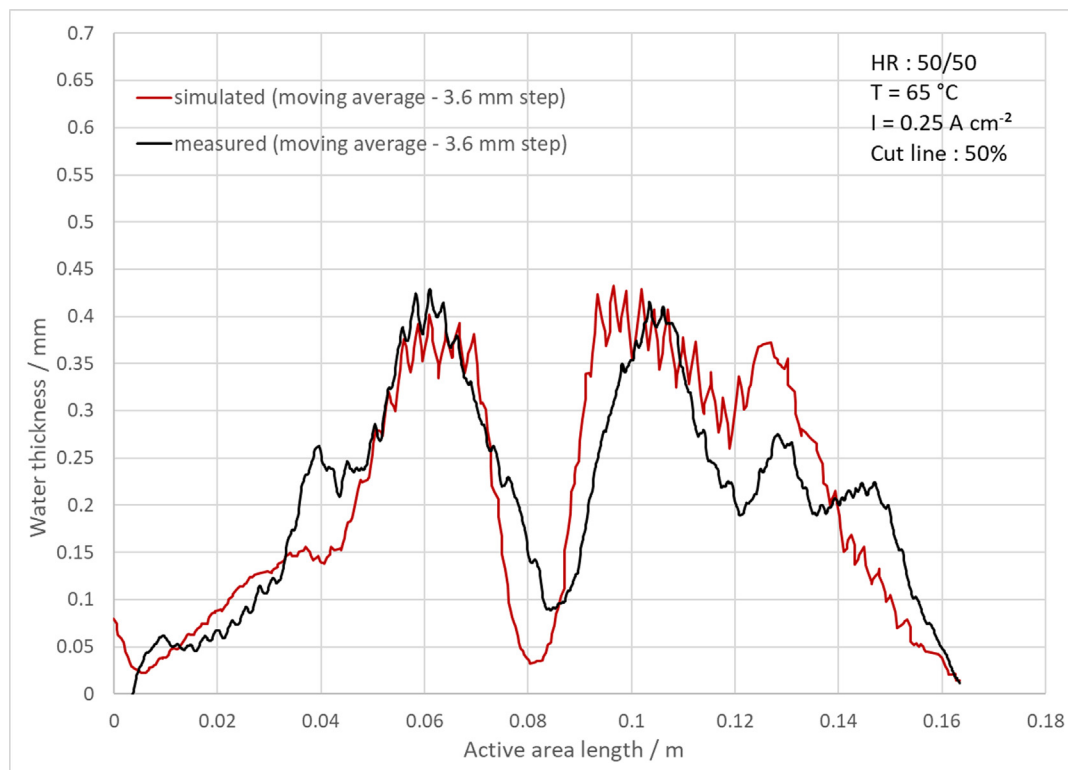


Fig. 6. Water thickness measured (black line) and simulated (red line) at the indicated 50% cut lines in the operating conditions presented in the Table 1 for a current density of 0.25 A cm^{-2} . (For interpretation of the references to color in this figure legend, the reader is referred to the web version of this article.)

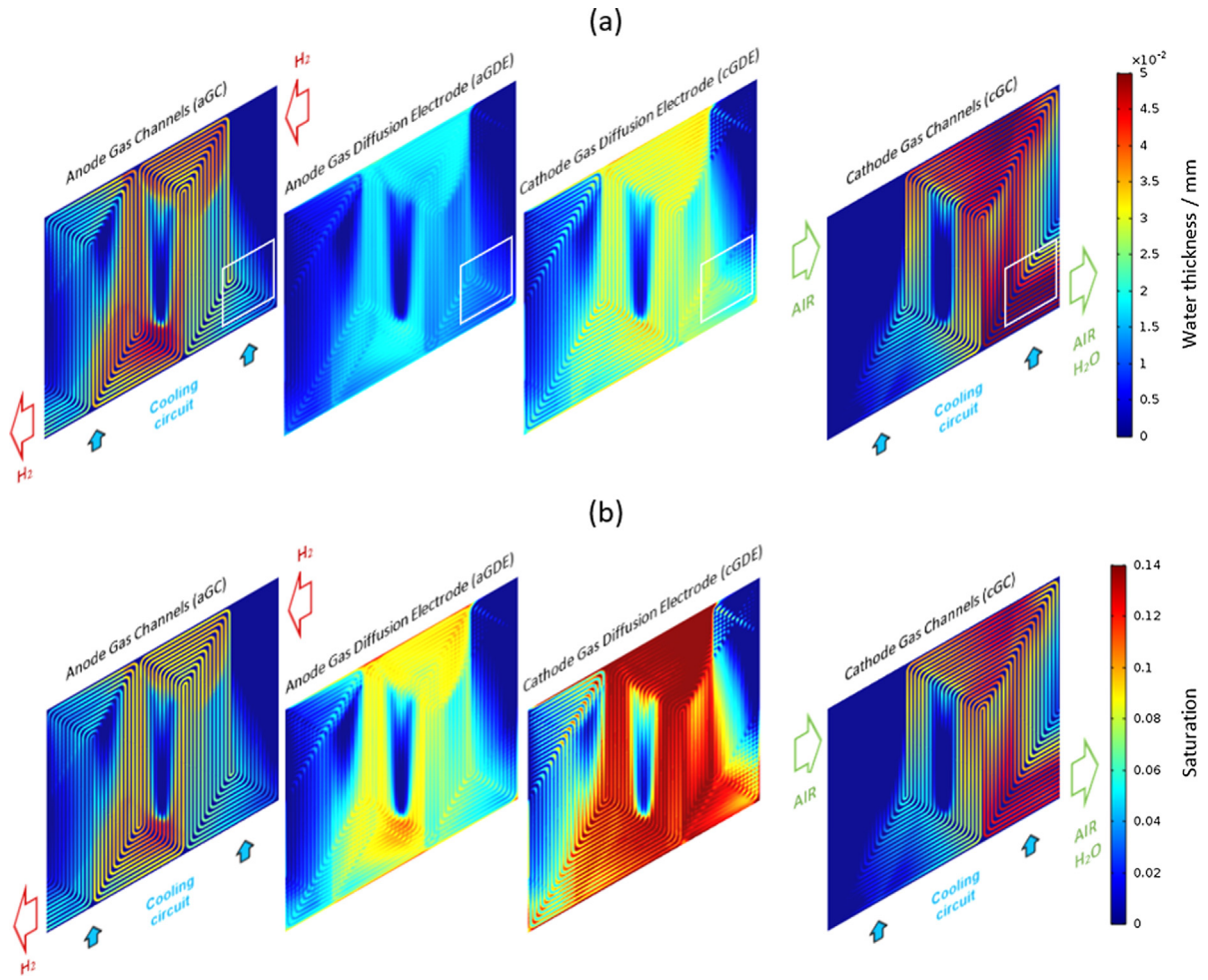


Fig. 7. (a) Water thickness and (b) saturation distribution in the anode and cathode gas channels and gas diffusion electrode, in the operating conditions presented in Table 1 for a current density of 0.25 A cm^{-2} and for humid conditions ($T = 65 \text{ }^\circ\text{C}$). The white boxes represent the zooms of Fig. 9a and b.

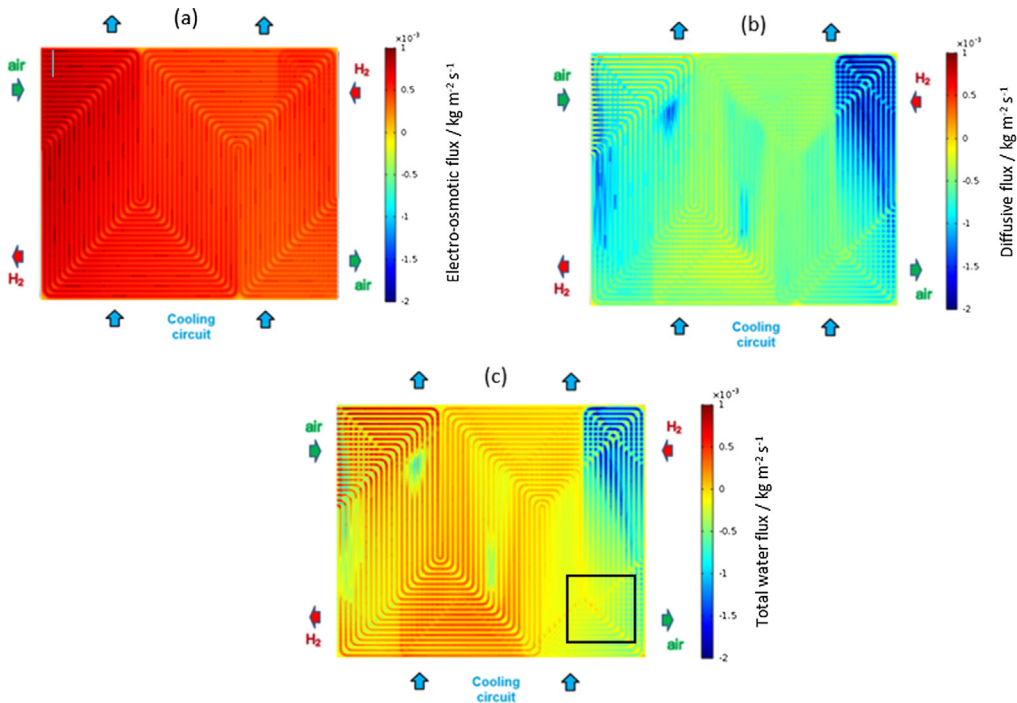
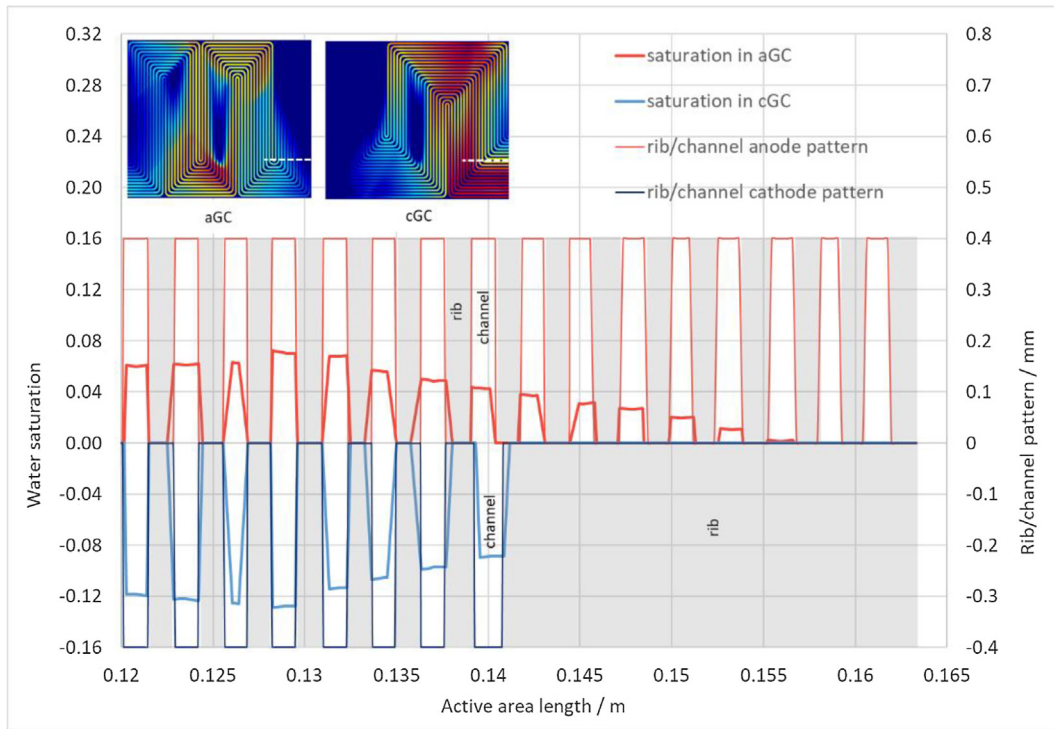


Fig. 8. Water fluxes through the membrane ($\text{kg m}^{-2} \text{ s}^{-1}$): (a) Electro-osmotic flux - (b) Diffusive flux - (c) Total water flux (Electro-osmotic flux + Diffusion). The black box represent the zoom of Fig. 9c.

(a)



(b)

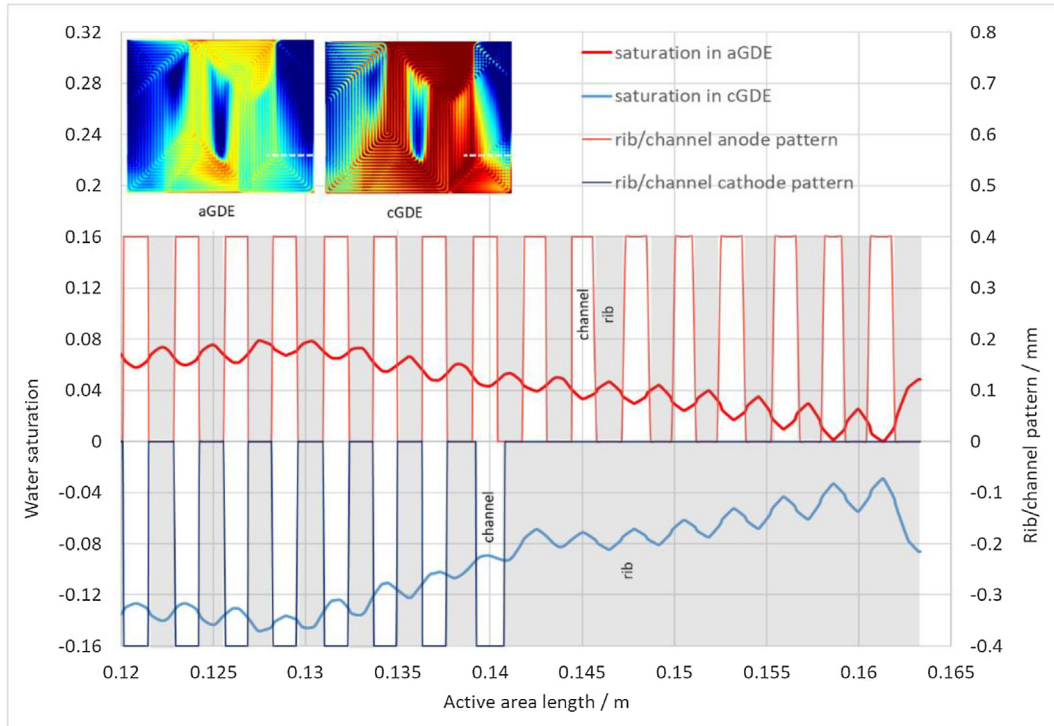


Fig. 9. Water thickness: (a) at the air outlet in GC – (b) at the air outlet in GDE – (c) Total water flux for humid conditions at 0.25 A cm^{-2} at the indicated 25% cut line.

(c)

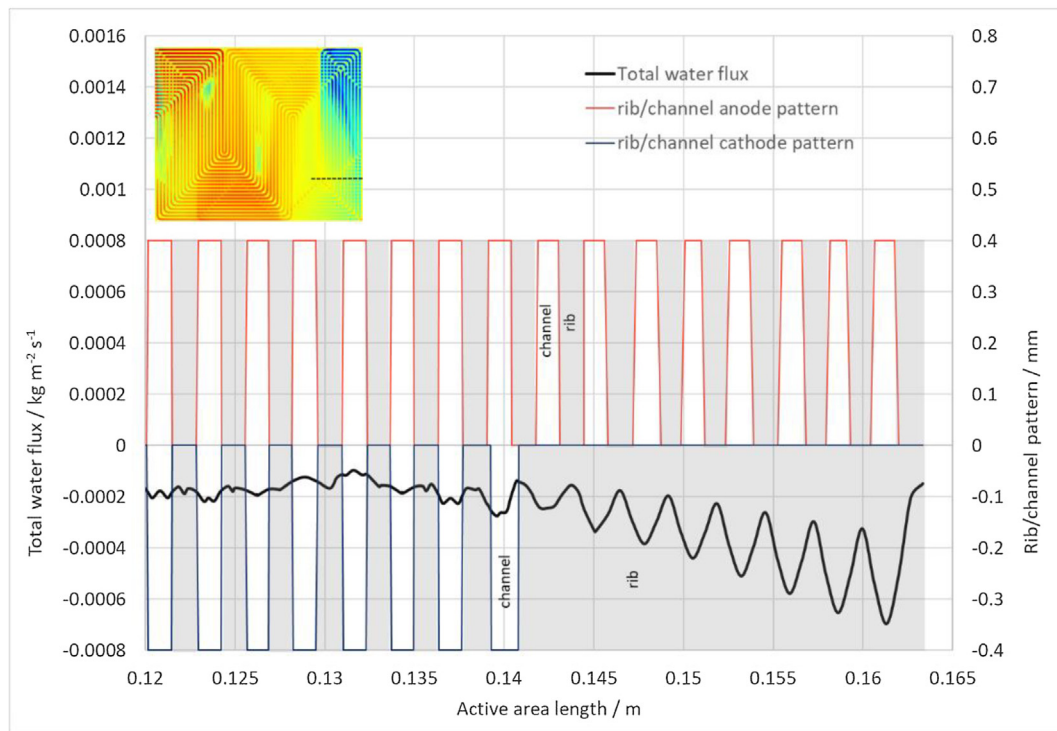


Fig. 9 (continued)

that the liquid water moves from the cathode to the anode by diffusion due to a higher liquid water concentration on the cathode side.

5. Conclusion

A pseudo-3D multiphysics model has been developed in previous work [29] to predict the temperature and humidity distributions of a large area PEMFC. The model has been validated for temperature and current intensity. It has been shown that the distribution is highly dependent on the local temperature directly related to the design of the cooling circuit. In this study, the model has been used to investigate the liquid water distribution. To do this, a two-phase flow simplification model has been implemented. To validate the model about the two-phase aspect, the results were compared to experimental tests by neutron imaging. Two current densities have been simulated to analyze their impact on the liquid water heterogeneities. The model is less accurate for higher current density for which there is paradoxically less liquid water. Nonetheless, the model is able to accurately locate and quantify the liquid water in the cell at lower current density. Once the model was validated for these conditions, the water distribution over the cell surface was studied in each layer in order to understand the water flux through the membrane. It appears that the liquid water accumulates in the cold zones and near the air outlet. To go further, a study was conducted at the rib/channel scale at low density current. It shows that the liquid water takes place preferentially under the rib in the GDE and the BP design has an important impact on the water distribution. Furthermore, the water transport properties of the membrane does not have a large impact on the overall distribution of water in the plane of the cell but is major factor ruling the local saturation in components. This study emphasizes the

complex distribution of water content and water flows at the inlet/outlet scale as well as the rib/channel scale. Indeed, there is no straightforward correlation between the operating conditions and the water management for the whole area of the cell. Thus, this makes the design of components, especially the GDE, to improve performance a tricky task without such type of 3D two-phase flow models.

That's why the domain validation was discussed by comparison between a classical model with phase-separated and the pseudo-3D model in order to validate the two-phase flow simplification. It can be concluded that the pseudo-3D model presents a good accordance for low saturation. Nevertheless, the validity domain cannot be defined precisely.

The main advantage of the pseudo-3D model is to obtain the liquid water, temperature and current distributions of a large cell scale in all components taking into account the real bipolar plate design. The model also allows to study precisely these parameters at a channel/rib scale in comparison with experimental methods often costly in time and money but also invasive and more or less accurate. The model can also be used to design innovative BP designs.

Declaration of Competing Interest

The authors declare that they have no known competing financial interests or personal relationships that could have appeared to influence the work reported in this paper.

Acknowledgements

This work was supported by the Communauté Université Grenoble Alpes. The authors extend their warmest thanks to

Prof. J. Fouletier, Dr J. Deseure and M. Henault for many fruitful discussions. We would also like to show our gratitude to S. Rosini, D.S. Hussey, D.L. Jacobson and J.M. LaManna for their precious help and expertise during the experimental tests. We also thank N. Martinez for developing an image processing software.

Appendix

The pressure drops obtained with the phase-separated and the pseudo-3D models are compared in this section.

A. Phase-separated model

With the phase-separated model, the phases are considered to be flowing separately in the channel, i.e. with different velocities. Each phase occupies a given fraction along the channel.

The empirical model proposed by Lockhart-Martinelli [44] is the original method to calculate the pressure drop caused by a two-phase flow in the mini-channels. The pressure drop can be expressed as (Eq. (25)):

$$\Delta P_1 = \phi_G^2 \Delta P_G \quad (25)$$

where ΔP_G and ϕ_G are respectively the pressure drop considering the gas phase flowing alone in the channel (Eq. (26)) and the two-phase multiplier.

$$\Delta P_G = 32 \mu_G \frac{\dot{m}_G}{\rho_G A_c} \frac{l}{d_c^2} \quad (26)$$

where A_c is the channel section, l is the channel length and d_c is the hydraulic diameter. For a laminar regime, the two-phase multiplier ϕ_G is defined by Eq. (27):

$$\phi_G^2 = 1 + CX + X^2 \quad (27)$$

where C is a parameter depending on the flow regime and X is the Martinelli's parameter. As discussed before, Lockhart-Martinelli [44] recommend $C = 5$. Others values are proposed in the literature as presented in the Section 3.3. The square Martinelli's parameter is the pressure drop ratio between the liquid and gas phase (Eq. (28)):

$$X^2 = \left(\frac{dP}{dz} \right)_L / \left(\frac{dP}{dz} \right)_G \quad (28)$$

The pressure drop ratio can be calculated classically and leads to Eq. (29):

$$X^2 = \frac{\mu_L \dot{m}_L}{\rho_L} \frac{\rho_G}{\mu_G \dot{m}_G} = \frac{\mu_L u_L}{\mu_G u_G} \frac{s_1}{1 - s_1} \quad (29)$$

Then, we can deduce the saturation of the phase-separated model (Eq. (30)) according to the Martinelli's parameter:

$$s_1 = \left(1 + \frac{u_G \mu_L}{u_L \mu_G X^2} \right)^{-1} \quad (30)$$

B. Pseudo-3D model

The pressure drop for the pseudo-3D model can be expressed as (Eq. (31)):

$$\Delta P_2 = 32 \mu_2 \frac{(\dot{m}_G + \dot{m}_L)}{\rho_2 A_c} \frac{l}{d_c^2} \quad (31)$$

where μ_2 and ρ_2 are respectively the moist air dynamic viscosity proposed by Wilke [52] and the moist air density defined as (Eq. (32)):

$$\rho_2 = \rho_{vap} s_2 + \rho_G (1 - s_2) \quad (32)$$

C. Relationship between the two saturations s_1 and s_2

The pressure drop of both models are considered equal, i.e. $\Delta P_1 = \Delta P_2$ and lead to Eq. (33):

$$\phi_G^2 = \frac{\Delta P_2}{\Delta P_G} = \frac{\mu_2 \rho_G}{\mu_G \rho_2} \left(\frac{u_G \rho_G (1 - s_2) + u_L \rho_L s_2}{u_G \rho_G (1 - s_2)} \right) \quad (33)$$

By replacing the moist air density ρ_2 in Eq. (34):

$$\phi_G^2 = \frac{\mu_2}{\mu_G} \frac{1}{1 - s_2} \quad (34)$$

Eq. (27) can be solved by having previously replaced the two-phase multiplier expression ϕ_G^2 (Eq. (35)). The Martinelli's parameter can then be expressed as a function of the pseudo-3D saturation s_2 (Eq. (36)).

$$X^2 + CX + 1 - \frac{\mu_2}{\mu_G} \frac{1}{1 - s_2} = 0 \quad (35)$$

$$X = \frac{1}{2} \left[-C + \sqrt{C^2 - 4 \left(1 - \frac{\mu_2}{\mu_G} \frac{1}{1 - s_2} \right)} \right] \quad (36)$$

Finally, the saturation s_1 described by the Lockhart-Martinelli model can be formulated according to the pseudo-3D saturation s_2 to obtain Eq. (37) already presented as Eq. (24) in the Section 3.3.

$$s_1 = \left(1 + \frac{u_G \mu_L}{u_L \mu_G X^2} \right)^{-1} = \left(1 + 4S \frac{\mu_L}{\mu_G} \left[-C + \sqrt{C^2 - 4 \left(1 - \frac{\mu_2}{\mu_G} \frac{1}{1 - s_2} \right)} \right]^{-2} \right)^{-1} \quad (37)$$

Supplementary material

Supplementary data to this article can be found online at <https://doi.org/10.1016/j.ijheatmasstransfer.2019.118720>.

References

- [1] DOE, Hydrogen and Fuel Cells Program 2018 Annual Merit Review and Peer Evaluation Report, <https://www.hydrogen.energy.gov/pdfs/review18/2018_amr_05_fuel_cell.pdf>, 2018.
- [2] Satish G. Kandlikar, Zijie Lu, Thermal management issues in a PEMFC stack – a brief review of current status, Appl. Therm. Eng. 29 (7) (2009) 1276–1280, <https://doi.org/10.1016/j.applthermaleng.2008.05.009>.
- [3] M. Ji, Z. Wei, A review of water management in polymer electrolyte membrane fuel cells, Energies 2 (2009) 1057–1106, <https://doi.org/10.3390/en20401057>.
- [4] F. Nandjou, J.-P. Poirot-Crouvezier, M. Chandresis, J.-F. Blachot, C. Bonnaud, Y. Bultel, Impact of heat and water management on proton exchange membrane fuel cells degradation in automotive application, J. Power Sources 326 (2016) 182–192, <https://doi.org/10.1016/j.jpowsour.2016.07.004>.
- [5] C. Fink, N. Fouquet, Three-dimensional simulation of polymer electrolyte membrane fuel cells with experimental validation, Electrochim. Acta 56 (28) (2011) 10820–10831, <https://doi.org/10.1016/j.electacta.2011.05.041>.
- [6] J.-P. Kone, X. Zhang, Y. Yan, G. Hu, G. Ahmadi, Three-dimensional multiphase flow computational fluid dynamics models for proton exchange membrane fuel cell: a theoretical development, J. Comput. Multiphase Flows 9 (1) (2017) 3–25, <https://doi.org/10.1177/1757482X17692341>.
- [7] C. Siegel, Review of computational heat and mass transfer modeling in polymer-electrolyte-membrane (PEM) fuel cells, Energy 33 (2008) 1331–1352, <https://doi.org/10.1016/j.energy.2008.04.015>.
- [8] N. Djilali, Computational modelling of polymer electrolyte membrane (PEM) fuel cells: challenges and opportunities, Energy 32 (2007), <https://doi.org/10.1016/j.energy.2006.08.007>.
- [9] A.Z. Weber, R.L. Borup, R.M. Darling, P.K. Das, T.J. Dursch, W. Gu, et al., A critical review of modeling transport phenomena in polymer-electrolyte fuel cells, J. Electrochem. Soc. 161 (2014) F1254–F1299, <https://doi.org/10.1149/2.0751412jes>.
- [10] A.Z. Weber, J. Newman, Modeling transport in polymer-electrolyte fuel cells, Chem. Rev. 104 (2004) 4679–4726, <https://doi.org/10.1021/cr0207291>.
- [11] K. Jiao, X. Li, Water transport in polymer electrolyte membrane fuel cells, Prog. Energy Combust. Sci. 37 (2011) 221–291, <https://doi.org/10.1016/j.peccs.2010.06.002>.

- [12] Y. Wang, K.S. Chen, J. Mishler, S.C. Cho, X.C. Adroher, A review of polymer electrolyte membrane fuel cells: technology, applications, and needs on fundamental research, *Appl. Energy* 88 (2011) 981–1007, <https://doi.org/10.1016/j.apenergy.2010.09.030>.
- [13] H. Meng, B. Ruan, Numerical studies of cold-start phenomena in PEM fuel cells: a review, *Int. J. Energy Res.* 35 (2011) 2e14, <https://doi.org/10.1002/er.1730>.
- [14] M. Secanell, J. Wishart, P. Dobson, Computational design and optimization of fuel cells and fuel cell systems: a review, *J. Power Sources* 196 (2011) 3690–3704, <https://doi.org/10.1016/j.jpowsour.2010.12.011>.
- [15] L.C. Pérez, L. Brandão, J.M. Sousa, A. Mendes, Segmented polymer electrolyte membrane fuel cells – a review, *Renew. Sustain. Energy Rev.* 15 (2011) 169–185, <https://doi.org/10.1016/j.rser.2010.08.024>.
- [16] Jens Eller, Tomas Rosén, Federica Marone, Marco Stampanoni, Alexander Wokaun, Felix Büchi, Progress in in situ X-ray tomographic microscopy of liquid water in gas diffusion layers of PEFC, *J. Electrochem. Soc.* 158 (2011) B963–B970, <https://doi.org/10.1149/1.3596556>.
- [17] L. Dubau, J. Durst, F. Maillard, M. Chatenet, L. Guétaz, J. André, E. Rossinot, Heterogeneities of aging within a PEMFC MEA, *Fuel Cells* 12 (2012) 188–198, <https://doi.org/10.1002/fuce.201100073>.
- [18] C.Y. Wang, Ping Cheng, A multiphase mixture model for multiphase, multicomponent transport in capillary porous media–I. Model development, *Int. J. Heat Mass Transf.* 39 (1996) 3607–3618, [https://doi.org/10.1016/0017-9310\(96\)00036-1](https://doi.org/10.1016/0017-9310(96)00036-1).
- [19] Weilin Zhuge, Yangjun Zhang, Pingwen Ming, Xingsheng Lao, Xiao Chen, Numerical simulation of three-dimensional gas/liquid two-phase flow in a proton exchange membrane fuel cell, *Front. Energy Power Eng. Chin.* 1 (2007), <https://doi.org/10.1007/s11708-007-0044-4>.
- [20] C. Siegel, Two-Dimensional, Non-Isothermal, Two-Phase Flow inside the Gas Diffusion Layer Unit of the Polymer-Electrolyte-Membrane Fuel Cell, in: *Proceedings of the COMSOL User Conference - Frankfurt, 2006*.
- [21] Z.H. Wang, C.Y. Wang, K.S. Chen, Two-phase flow and transport in the air cathode of proton exchange membrane fuel cells, *J. Power Sources* 94 (1) (2001) 40–50, [https://doi.org/10.1016/S0378-7753\(00\)00662-5](https://doi.org/10.1016/S0378-7753(00)00662-5).
- [22] Wensheng He, Jung Yi, Trung Nguyen, Two-phase flow model of the cathode of PEM fuel cells using interdigitated flow fields, *AIChE J.* 46 (2000) 2053–2064, <https://doi.org/10.1002/aic.690461016>.
- [23] Yun Wang, Suman Basu, Chao-Yang Wang, Modeling two-phase flow in PEM fuel cell channels, *J. Power Sources* 179 (2008) 603–617, <https://doi.org/10.1016/j.jpowsour.2008.01.047>.
- [24] Suman Basu, Chao-Yang Wang, Ken Chen, Phase change in a polymer electrolyte fuel cell, *J. Electrochem. Soc.* 156 (2009) B748, <https://doi.org/10.1149/1.3115470>.
- [25] M. Andersson, S.B. Beale, M. Espinoza, Z. Wu, W. Lehnert, A review of cell-scale multiphase flow modeling, including water management, in polymer electrolyte fuel cells, *Appl. Energy* 180 (2016) 757–778, <https://doi.org/10.1016/j.apenergy.2016.08.010>.
- [26] Tomasz Bednarek, Georgios Tzotridis, Issues associated with modelling of proton exchange membrane fuel cell by computational fluid dynamics, *J. Power Sources* 343 (2017) 550–563, <https://doi.org/10.1016/j.jpowsour.2017.01.059>.
- [27] Pierre Oberholzer, Pierre Boillat, Local characterization of PEFCs by differential cells: systematic variations of current and asymmetric relative humidity [J. Electrochem. Soc., 161, F139 (2014)], *J. Electrochem. Soc.* 161 (2014) X7–X7, <https://doi.org/10.1149/2.100403jes>.
- [28] Joseph D. Fairweather, Dusan Spornjak, Adam Weber, David Harvey, Silvia Wessel, Daniel L. Hussey, David Jacobson, Kateryna Artyushkova, Rangachary Mukundan, Rodney L. Borup, Effects of cathode corrosion on through-plane water transport in proton exchange membrane fuel cells, *J. Electrochem. Soc.* 160 (2013). F980–F993. [10.1149/2.024309jes](https://doi.org/10.1149/2.024309jes).
- [29] F. Nandjou, J.-P. Poirot-Crouvezier, M. Chandesris, Y. Bultel, A pseudo-3D model to investigate heat and water transport in large area PEM fuel cells – Part 1: model development and validation, *Int. J. Hydrogen Energy* 41 (34) (2016) 15545–15561, <https://doi.org/10.1016/j.ijhydene.2016.05.117>.
- [30] F. Nandjou, J.-P. Poirot-Crouvezier, M. Chandesris, S. Rosini, D.S. Hussey, D.L. Jacobson, J.M. LaManna, A. Morin, Y. Bultel, A pseudo-3D model to investigate heat and water transport in large area PEM fuel cells – Part 2: application on an automotive driving cycle, *Int. J. Hydrogen Energy* 41 (34) (2016) 15573–15584, <https://doi.org/10.1016/j.ijhydene.2016.06.007>.
- [31] Omid Babaie Rizvandi, Serhat Yesilyurt, A pseudo three-dimensional, two-phase, non-isothermal model of proton exchange membrane fuel cell, *Electrochim. Acta* 302 (2019) 180–197, <https://doi.org/10.1016/j.electacta.2019.02.018>.
- [32] D.S. Hussey, D.L. Jacobson, M. Arif, K.J. Coakley, D.F. Vecchia, In situ fuel cell water metrology at the NIST Neutron Imaging Facility, *ASME J Fuel Cell Sci Technol* 7 (2010) 21–24.
- [33] D.S. Hussey, D.L. Jacobson, High resolution of neutron radiography analysis of proton exchange membrane fuel cells, in: U. Pasaogullari, C.Y. Wang (Eds.), *Modeling and diagnostics of fuel cells*, Springer, New York, 2010, pp. 175–199.
- [34] T.A. Trabold, J.P. Owejan, J.J. Gagliardo, D.L. Jacobson, D.S. Hussey, M. Arif, Use of neutron imaging for proton exchange membrane fuel cell (PEMFC) performance analysis and design, in: *Handbook of fuel cells: advances in electrocatalysis, materials, diagnostics and durability*, 2010.
- [35] T.A. Trabold, J.P. Owejan, J.J. Gagliardo, D.L. Jacobson, D.S. Hussey, M. Arif, Use of neutron imaging for proton exchange membrane fuel cell (PEMFC) performance analysis and design, in: W. Vielstich, A. Lamm, H. Gasteiger (Eds.), *Handbook of Fuel Cells Fundamentals, Technology, Application*, Wiley, New York, 2003, pp. 658–673.
- [36] M. Kaviany, *Principles of Heat Transfer in Porous Media*, Springer, New York, 1991.
- [37] T.E. Springer, T.A. Zawodzinski, S. Gottesfeld, Polymer electrolyte fuel cell model, *J. Electrochem. Soc.* 138 (8) (1991) 2334–2342.
- [38] S. Hwang, P. Lee, S. Jo, C. Cha, S. Hong, S. Han, J. Ko, Transient behavior of proton exchange membrane fuel cell under non-isothermal condition, *Renew. Energy* 42 (2012) 54–59.
- [39] F. Meier, G. Eigenberger, Transport parameters for the modelling of water transport in ionomer membranes for PEM-fuel cells, *Electrochim. Acta* 49 (2004) 1731–1742.
- [40] T. Zawodzinski, J. Dawy, J. Valerio, S. Gottesfeld, The water content dependence of electroosmotic drag in proton-conducting polymer electrolytes, *Electrochim. Acta* 40 (1994) 297–302.
- [41] Fuller, Solid-polymer electrolyte fuel cells, PhD Dissertation, University of California, 1992.
- [42] T. Zawodzinski, M. Neeman, L. Sillerud, S. Gottesfeld, Determination of water diffusion coefficient in perfluorosulfonate ionomeric membranes, *J. Phys. Chem.* 95 (1991) 6040–6044.
- [43] S. Motupally, A. Becker, J.W. Weidner, Diffusion of water in Nafion 115 membranes, *J. Electrochem. Soc.* 147 (9) (2000) 3171–3177.
- [44] R.W. Lockhart, R.C. Martinelli, Proposed correlation of data for isothermal two-phase, two-component flow in pipes, *Chem. Eng. Prog.* 45 (1949) 38–48.
- [45] D. Chisholm, A theoretical basis for the Lockhart-Martinelli correlation for two-phase flow, *Int. J. Heat Mass Transf.* 10 (12) (1967) 1767–1778.
- [46] S.-M. Kim, I. Mudawar, Universal approach to predicting two-phase frictional pressure drop for adiabatic and condensing mini/micro-channel flows, *Int. J. Heat Mass Transf.* 55 (2012) 3246–3261.
- [47] K. Mishima, T. Hibiki, Some characteristics of air–water two-phase flow in small diameter vertical tubes, *Int. J. Multiphase Flow* 22 (1996) 703–712.
- [48] W. Zhang, T. Hibiki, K. Mishima, Correlations of two-phase frictional pressure drop and void fraction in mini-channel, *Int. J. Heat Mass Transfer* 53 (2010) 453–465.
- [49] W. Li, Z. Wu, A general correlation for adiabatic two-phase pressure drop in micro/mini-channels, *Int. J. Heat Mass Transfer* 53 (2010) 2732–2739.
- [50] Y.S. Muzychka, M.M. Awad, Asymptotic generalizations of the Lockhart–Martinelli method for two phase flows, *J. Fluids Eng.* 132 (2010) 0313021–313112.
- [51] B. Straubhaar, J. Pauchet, M. Prat, Pore network modelling of condensation in gas diffusion layers of proton exchange membrane fuel cells, *Int. J. Heat Mass Transf.* 102 (2016) 891–901, <https://doi.org/10.1016/j.ijheatmasstransfer.2016.06.078>.
- [52] C.R. Wilke, A viscosity equation for gas mixtures, *J. Chem. Phys.* 18 (1950) 517–519.